Feedback-free microfluidic oscillator with impinging jets

A. Bertsch[1], A. Bongarzone[2], M. Duchamp[1], P. Renaud[1], F. Gallaire[2]

[1]*Microsystems Laboratory LMIS4, École Polytechnique Fédérale de Lausanne, Lausanne, CH-1015, Switzerland,*

[2]*Laboratory of Fluid Mechanics and Instabilities, École Polytechnique Fédérale de Lausanne, Lausanne, CH-1015, Switzerland*

Abstract

The present paper describes a microfluidic oscillator, based on facing impinging jets and operating in laminar flow conditions. Using appropriate microchannel configurations, pulsatile liquid flows are generated at the microscale from steady and equal inlet flow conditions and without moving parts or external stimuli. An experimental campaign has been carried out, using oscillator structures manufactured in silicon using conventional microfabrication techniques. This allowed to study in detail the impact of the main geometric parameters of these structures on the oscillation frequency. The observed range of regular oscillations was found to depend on the geometry of the output channels, with highly regular oscillations occurring over a very large range of Reynolds numbers (Re) when an expansion of the output channel is added. The evolution of the self-oscillating frequency was shown to be dependent on the distance separating the impinging jets and on the average speed of the jets. Direct numerical simulations (DNS) have been performed using a spectral element method. The computed dye concentration fields and non-dimensional self-oscillation frequencies compare well with the experiments. The simulations enable a detailed characterization of the self-oscillation phenomenon in terms of pressure and velocity fields.

I. INTRODUCTION

Fluidic oscillators are a set of devices that issue an oscillating jet of fluid when supplied with a continuous stream of pressurized gas or liquid. They started to be studied in the 1960s, as well as other fluidic devices functioning with no moving parts, such as fluidic logic elements or fluidic amplifiers [1–3]. There are two main types of fluidic oscillators, wall-attachment devices and jet interaction devices. The wall-attachment oscillators are based on the Coandă effect, where the fluid jet interacts with an adjacent wall, which results in its deflection. The jet interaction devices also named ”feedback-free” devices are based on the interactions of two jets inside an interaction chamber having a specific geometry [4]. Only a few industrial applications of fluidic oscillators have emerged over the years, such as flow metering [5] and windshield washer devices [6], however, with the development of microfluidics and its applications to lab-on-chip devices, a renewed interest for fluidic devices appeared, and in particular for fluidic devices with no moving parts, such as static micromixers [7] or fluidic diodes [8–10].

Most research work performed so far on microfluidic oscillators operating with liquids aims either at the study of new types of static micromixers or at the implementation of fluidic logic circuits. A small number of such fluidic oscillators have been described in the scientific literature, and implement a variety of working principles.

Notwithstanding active microfluidic oscillators have been studied [11], here we mainly focus on passive oscillators, where a constant liquid flow is applied at the inlets and oscillations are generated by the design of the microfluidic network. One of the most studied type of microfluidic oscillators is based on the use of fluidic resistors, capacitors and valves, and uses the analogy between the electrical and fluidic domains, where voltage is replaced by pressure and electrical current is replaced by hydraulic volume flow. The microfluidic equivalent of electrical resistors are channels, microfluidic capacitors are chambers with membranes that store the energy by membrane deformation, diodes and transistors equivalents are valves of diverse designs that can completely shut off the flow in given conditions. Based on this electronic-fluidic analogy, a fluidic astable multivibrator driven by a constant pressure flow was described by Lammerink *et al.* [12]. This concept was further developed later, taking advantage of the versatility of the microfabrication methods based on the use of polydimethylsiloxane (PDMS), an elastomeric material that renders the fabrication of fluidic networks containing membranes very simple. Mosadegh *et al.* [13] demonstrated a microfluidic oscillator and used it to perform flow switching and clocking functions. Kim *et al.* fabricated a number of devices based on this type of microfluidic oscillator [14, 15] such as a micromixer [16] and an autonomous pulsed flow generation system capable of generating on demand and independently a range of flow rates and a range of flow oscillation frequencies, and applied it in studying endothelial cell elongation response to fluidic flow patterns [17]. Devaraju *et al.* also demonstrated a fluidic oscillator, among many other fluidic logic functions [18] and Nguyen *et al.* performed peristaltic pumping on chip using a control signal generated on chip through a fluidic oscillator circuit [19].

Xia *et al.* also developed a micromixer based on a vibrating elastomeric diaphragm trapped in a two-level cavity. Here, there is no need of a complex fluidic circuit as the deformation of the diaphragm directly creates the oscillating liquid flow, but the wear of the elastomeric material limited the use of this device [20]. Simpler microfluidic oscillators containing no moving parts, no deformable membranes and no complex fluidic circuit have also been studied by several authors. These oscillators are based on jets interacting in a simple cavity and generating an oscillating flow [21, 22]. Yang *et al.* [23] demonstrated that feedback-driven microfluidic oscillators based on the Coandă effect can generate an oscillatory liquid flow at small Reynolds numbers. Their design used a micro-nozzle with a sudden expansion and asymmetric feedback channels and measured oscillatory frequencies of the flow below $1\,Hz$ for Reynolds numbers between 1 and 100. Similar oscillator designs were later studied experimentally by Xu *et al.* [24] to develop feedback micromixers based on the Coandă effect. They demonstrated that there were three different oscillating mechanisms that resulted in mixing in such structures, depending on the magnitude of the Reynolds number: vortex mixing, internal recirculation mixing, and oscillation mixing. Xie et al. [25] simulated the fluidic behavior of such devices using the Fluent® CFD software.

Finally, Sun *et al.* [26, 27] studied liquid mixing resulting from a microfluidic oscillator using an impinging jet on a concave semi-circular surface. This type of microfluidic oscillator is another example of use of the Coandă effect. Oscillations were observed for Reynolds numbers as low as 70, with the frequency of oscillations below $1\,Hz$.

We present here a microfluidic oscillator that can be classified in the jet interaction device category. It has a very simple configuration and its oscillations depend on the jet interactions more than on the shape of the surrounding cavity. This device is based on facing impinging liquid jets and operates in laminar flow conditions. Observations of flow patterns obtained with micromixers having geometries similar to the ones presented in this paper but much larger dimensions were performed by Tesař [28], however, the manufacturing method of these devices limited their aspect ratios and allowed to perform observations of only a limited part of the phenomenon. Impinging self-oscillating jets have been described in scientific literature by Denshchikov *et al.* [29] using facing turbulent water jets, having dimensions in the centimeter range immersed in a 230L water tank. In a follow-up paper [30], the period of the auto-oscillating phenomenon was empirically described by a set of equations. If the phenomena described in the present paper shows some similarities with the jet configuration presented in [29, 30], the jets dimensions are orders of magnitude smaller and the flow conditions remain laminar [31].

II. MICROFLUIDIC DEVICES, FABRICATION AND EXPERIMENT DESCRIPTION

The oscillator structures presented in the present paper were fabricated using conventional microfabrication technologies in standard conditions. The fabrication process is very simple and did not require any particular development. It is based on the use of the Bosch process to create small components with a high aspect-ratio, but various other microfabrication processes could have been successfully used for fabricating such simple structures.

A $10\,cm$ in diameter double-side polished silicon wafer was first bonded to a glass wafer by anodic bonding ($800V$, $420°C$). The silicon part will be patterned to form the fluidic network, while the glass layer both supports these structures and will later allow observation using an inverted optical microscope. When necessary, the thickness of the silicon wafer was reduced by grinding. The silicon surface of the bonded wafers was then coated with a thick layer of positive photoresist (AZ9260, $10\,\mu m$) and patterned by direct writing (MLA150, Heidelberg Instruments). The patterned silicon was etched using the Bosch process, until the glass layer is reached (Adixen AMS200, Alcatel Micro Machining Systems). During this step, the full thickness of the silicon wafer is etched, as well as part of the photoresist masking layer. The cavities created with the Bosch process will constitute the microchannels, inlets and outlets of the fluidic network. The remains of the photoresist mask are finally striped using O_2 plasma ($10\,min$, $500\,W$) and the wafers are diced into chips. Each of the fabricated chips is closed by a 5mm thick flat slab of polydimethylsiloxane (PDMS) in which inlet and

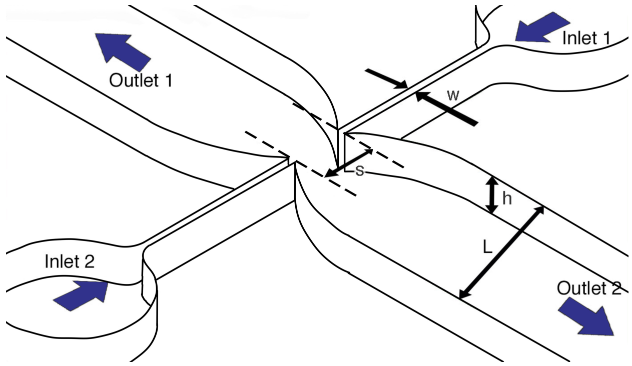

Figure 1. Three-dimensional sketch of a general oscillator structure.

outlet holes are made using a 0.75 mm in diameter puncher. The PDMS cover is placed on top of the silicon surface of the diced chips after submitted both components to an oxygen plasma, which results in an adequate bonding of the two components.

A schematic diagram of the design of the fabricated components is presented in Fig. 1. The liquid enters the device by two inlets and is pushed through long and narrow facing channels of width w towards a wider transverse channel. The narrow entry channels, whose length are at least 2.3 mm each, act as two nozzles separated by a distance s to create two facing liquid jets when they reach the larger lateral channel. Outlets are provided at both ends of the large channel, far away from the intersection. The outlet channel extends over the entire length of the manufactured chip and the liquid exits the chip at a distance of 8 mm from the facing nozzles. Within this geometry, the Reynolds number can be defined as:

$$Re = \frac{\rho U w}{\mu}, \tag{1}$$

where ρ is the fluid density, μ is its dynamic viscosity, U is the average velocity of the liquid flow at the nozzles. In a certain range of Reynolds numbers, these colliding jets do self-oscillate transversally into the two output channels. Away from the nozzles, the width of the output channels quickly increases to a constant value L, in the most general case, but experiments have also been performed with two simple intersecting straight channels ($L = s$). When an expansion of the outlet channel is provided ($L \neq s$) the full width of the outlet channel is reached at a distance of $0.75L$ away from the nozzle, and the wall profile in this area is a circular arc, tangent to the outlet channel wall and joining the nozzle. The height h of the walls is constant for the whole device.

The microfluidic devices were placed with their glass side facing down on the stage of an inverted microscope. Fluidic connections were made through the PDMS top layer by inserting $0.79\,mm$ in outer diameter PEEK tubes of equal length in the inlet holes. Deionized water colored with two different food dyes was pushed through the two inlet tubes using a syringe pump (PHD2000, Harvard apparatus). The syringe pump accommodated two identical syringes that were actuated simultaneously. The outlet holes on the PDMS cover were also fitted with PEEK tubes of identical length, and the liquid flow coming out of them was discarded. With the syringe pumps used, flow rates up to $20\,mL/min$ could be obtained in each of the entry channels, depending on the overall flow resistance of the studied microfluidic device. During experiments, the flow rates were changed abruptly, without ramps. Experiments were carried out in which the flow rates were first increased and later decreased, but no hysteresis in the evolution of the oscillation frequency with Reynolds was observed. Observations were made using a 10x microscope objective in bright field conditions, and recorded using a high-speed camera (Miro M 310, Phantom). The resolution, frame rate and gain of the camera was chosen for each experiment such that the frequency of the microfluidic oscillators could be clearly observed and measured using a large number of frames. As the microscope light source illuminates the complete microchannel height, the recorded light intensity provides a depth averaged concentration field.

To evaluate the effect of the length of the entry channel on the oscillator behavior and make sure that the observed oscillations were not an artefact related to the inlet flow profile, multiple identical oscillator cavities differing only in the lengths of the inlet channel were manufactured, with an inlet channel varying between $0.45\,mm$ and $8.35\,mm$ in the length and an inlet width of $100\,\mu m$ (a ratio between 4.5 and 83.5 respectively). The evolution of the frequency with Re was measured in each configuration and showed no difference from chip to chip, indicating that the oscillator behavior is not influenced by the inlet channel length, at least in the geometries investigated in the present paper. This justified conducting all other experiments with an inlet channel length of $2.3\,mm$.

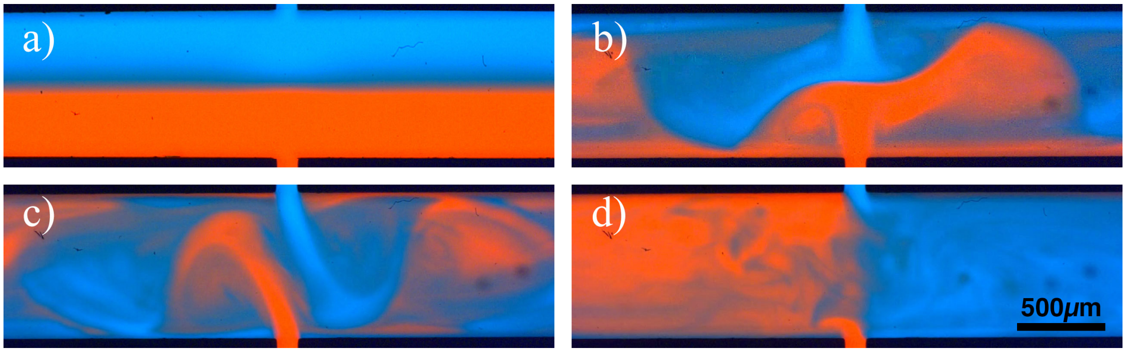

Figure 2. Images of the oscillating flow observed for increasing values of the Reynolds number for $h = 525\,\mu m$, $w = 100\,\mu m$, $s = 800\,\mu m$, $L = 800\,\mu m$: *a*) $Re = 15$, no oscillations. *b*) $Re = 23$, $F = 27\,Hz$, slow oscillations. *c*) $Re = 31$, $F = 43\,Hz$, alternating jets. *d*) $Re = 95$, Jets do not cross regularly (see movie S1 in Supplemental Material [32]).

III. EXPERIMENTAL RESULTS

A. Oscillations in simple straight channels and in channels with expansion

Fig. 2 shows images extracted from high-speed videos, visualizing the water flow colored with two food dyes in a structure made of straight channels crossing at right angle. Inlet channels are $w = 100\,\mu m$ in width, the two nozzles are $s = 800\,\mu m$ apart, outlet channels are $L = 800\,\mu m$ in width. The height of all channels is $h = 525\,\mu m$. There is no expansion of the output channels in this design ($s = L$). For low values of the Reynolds number steady flow conditions are present (Fig. 2-*a*), the flow of both dyes is steady and the boundary between fluids is stable with time. When Re increases and reaches a value of about 20, the two flows start to oscillate in an antisymmetric way, with both jets first bifurcating in opposite directions, and later coming back towards one another until they collide and switch sides. Fig. 2-*b* shows oscillations at $Re = 23$. They have a low frequency, are very regular temporally and spread widely in the lateral output channels. For larger values of Re, clear alternating arrow-shaped jets oscillating very regularly can be observed (Fig. 2-*c*).

Their oscillating frequency increases with Re. When Re reaches a threshold value of about $Re_{irr} = 90$, the regularity is lost and the flow evolves into a complex, irregular and aperiodic regime (Fig. 2-*d*). Little mixing occurs between the liquid coming from each of the two jets, and each output channel contains mostly the liquid originating from one of the

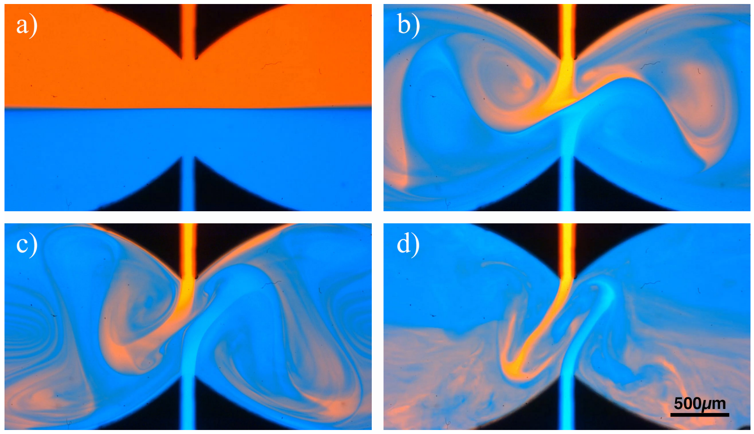

Figure 3. Images of the oscillating flow observed for different values of the Reynolds number for $h = 525\,\mu m$, $w = 100\,\mu m$, $s = 800\,\mu m$, $L = 2000\,\mu m$: *a*) $Re = 15$, no oscillations. *b*) $Re = 23$, $F = 32\,Hz$ slow oscillations. *c*) $Re = 31$, $F = 53\,Hz$ large oscillations resulting in a stretching and folding of the liquid flows. *d*) $Re = 158$, $F = 362\,Hz$, fast oscillations with arrow-shaped jets, but resulting in an apparently less efficient mixing of the two liquids (see movie S2 in Supplemental Material [32]).

jets only. From time to time oscillations of the jets do occur, but without following a regular temporal switching pattern.

Fig. 3 illustrates the evolution of the flow with Re in a configuration that is exactly the same as the one presented in Fig. 2, except for the exit channels that do present an expansion in their width: the two nozzles are still $800\,\mu m$ apart, but the width of the exit channel quickly increases to $L = 2\,mm$. For low values of Re, Stokes flow conditions are observed (Fig. 3-*a*), with a steady boundary between the flows emerging from each inlet. When Re increases, symmetric oscillations still start to occur for a value of Re of about 20. Fig. 3-*b* shows oscillations observed for $Re = 23$. When Re is further increased, the oscillation frequency also increases. Large oscillations having dimensions similar to the distance between the jets are observed and result in a stretching and folding of the liquid flows (Fig. 3-*c*).

Regular oscillations of the two impinging jets were observed until $Re = 630$, where the experiment was stopped as the used syringe pumps could not provide a larger flow rate. As shown in Fig. 3-*d*, high values of Re induce fast oscillations of the two liquid flows, with arrow-shaped jets, but the oscillations lateral amplitude reduces. The stretching and folding of the fluid flow is of lesser magnitude than in the case of Fig. 3-*c*, as most of the liquid

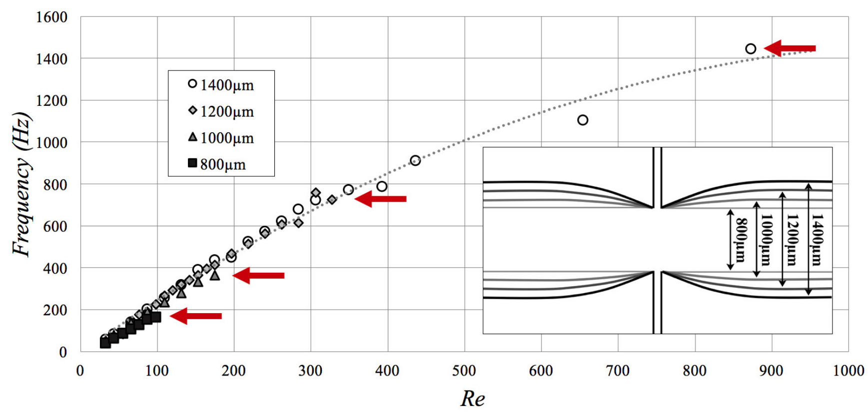

Figure 4. Evolution of the oscillation frequency with Re for the four channel designs presented in the insert, showing the same configuration except for the output channels that do present different expansions in their widths. For all designs, $h = 380\,\mu m$, $w = 100\,\mu m$, $s = 800\,\mu m$. The larger the output channel, the larger the range of Re for which oscillations are stable. The dotted line is drawn only to guide the eye. The red arrows indicate the end of the stable oscillation regime for each value of the output channel width.

issued from one nozzle is strongly pushed towards the opposite side of the exit channel. The comparison of the oscillations resulting from identical designs with and without expansion in the exit channel shows that the threshold at which oscillations start in both cases, occurs for similar values of the Re number. The oscillation frequency observed is slightly higher when an expansion channel is present. More importantly, the impinging jets oscillate with high regularity for a much wider range of Reynolds numbers when an expansion of the exit channel is provided.

Fig. 4 shows the evolution of the oscillation frequency for four oscillator designs having the same configuration ($h = 380\,\mu m$, $w = 100\,\mu m$, $s = 800\,\mu m$) except that they present different widths in their output channels, as schematically presented in the figure insert. In all cases, the value of Re at the threshold for which oscillations start is the same, but the larger the output channel, the larger the range of Re for which regular operation can be maintained, i.e. Re_{irr} increases. .

Moreover, the oscillation frequency at a given value of Re is slightly smaller for designs presenting a smaller width in their output channel. If self-oscillations occur for low values of Re in simple straight crossing channels of adequate dimensions, providing an expansion in the output channel allows to stabilize the oscillation mechanism and extends the oscillation regime over a wider range of Re, with only a minor effect on the frequency of oscillations. The extension of the oscillation regime between straight channels and channels presenting an expansion has been observed in all cases, regardless of the height h of the oscillator structure.

B. Flow patterns created in the exit channels

Fig. 5 shows the liquid flow close to the oscillator and further away laterally in one of the two output channels for $h = 525\,\mu m$, $w = 100\,\mu m$, $s = 400\,\mu m$, $L = 2000\,\mu m$. For low values of Re (Fig. 5-a and b), the amplitude of the oscillations is limited and smaller than the distance s separating the two inlets. As the liquid is pushed in the expanding part of the exit channels, the pattern of the two fluids resulting from these oscillations is stretched along the channel width, resulting in temporal alternations of the fluids coming from the inlets. This appears as regularly spaced blue and red stripes of fluid in Fig. 5-a and b. When Re increases, the oscillations become arrow-shaped jets of fluid, and the liquid issued from each nozzle is pushed towards the opposite side of the channel (Fig. 5-c). Further away in the exit channels, the fluid flow is rearranged but remains segmented in two parts because of the laminar flow conditions, each part showing a temporal alternation of both fluids with however a unequal ratio with a prevalence in each branch of one fluid with respect to the other, but not with equal ratios (Fig. 5-d). If the temporal alternation of the fluid observed for low values of Re provides conditions of interest for microscale fluid mixing, it is not the case for the conditions created for larger values of Re, where the fluid flow remains segmented and only a limited mixing of the two fluids is expected in each of its parts. We have not further investigated the mixing efficiency from a quantitative point of view.

C. Evolution of the frequency with the oscillator geometry

The three main geometric parameters that may influence the self-oscillation phenomenon are the width of the jets w, the distance between the jets s and the height of the device h. Fig. 6-a shows the evolution of the frequency with Re, for different values of the jets width, all other geometric dimensions being identical across all devices ($h = 525\,\mu m$, $s = 500\,\mu m$, $L = 2000\,\mu m$). For a given value of the jets width, the oscillation frequency increases with Re, and at a chosen value of Re, the oscillation frequency increases when the jet width

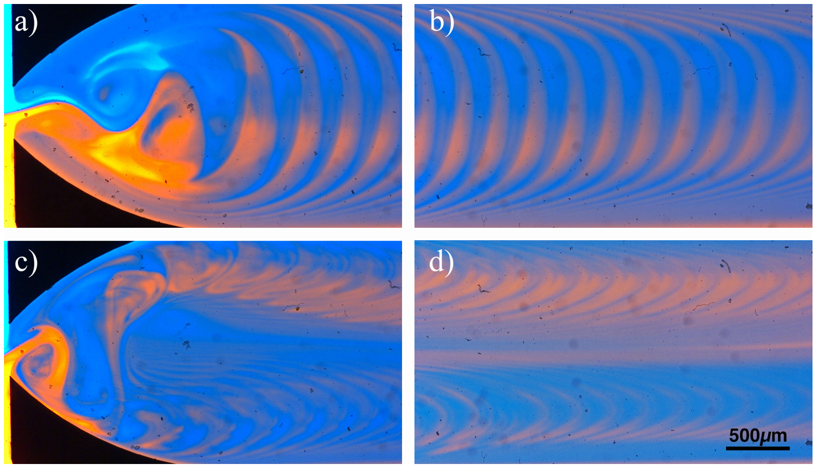

Figure 5. Images of the flow close to the oscillator (a and c) and further away laterally in one of the two output channels (b and d) for $h = 525\,\mu m$, $w = 100\,\mu m$, $s = 400\,\mu m$, $L = 2000\,\mu m$: *a*) and *b*) correspond to $Re = 35$, $F = 120Hz$, a temporal rearrangement of the fluid is observed. *c*) and *d*) correspond to $Re = 47$, $F = 165\,Hz$, next to the oscillator a dead zone is visible where the fluid is stagnant. Further away, this dead zone gradually disappears but the fluid flow remains segmented in two parts, each part showing a temporal alternation of both inlet fluids, but not with equal ratios (see movie S3 in Supplemental Material [32]).

decreases. The threshold at which the oscillations appear is reached for smaller Re when the width of the jet is smaller. Colliding jets of identical design, having a width of $300\,\mu m$ were also tested but oscillations of the fluid flows could not be observed. For the jets width of 150 and $200\,\mu m$, the range of Re where oscillations occur is limited: in both cases the threshold where oscillations start is close to $Re = 50$, and the flow stops to oscillate and gives way to a stable flow pattern similar to the one observed by Haward *et al.* [9] when another threshold Re number is reached (in the order of $Re = 250$ for $w = 200\,\mu m$ and $Re = 290$ for $w = 150\,\mu m$). For smaller values of the jets width, regular and symmetric oscillations of the two impinging jets were observed until values of Re close to 600. Flow conditions for larger values of Re could not be investigated as the syringe pumps used could not deliver larger flow rates. Oscillators having jets width smaller than $50\,\mu m$ were not manufactured in the frame of this experiment, but other experiments we performed indicate that oscillations can be expected to occur for much smaller values of the jets width.

Fig. 6-*b* shows the evolution of the frequency with Re, when the distance between the

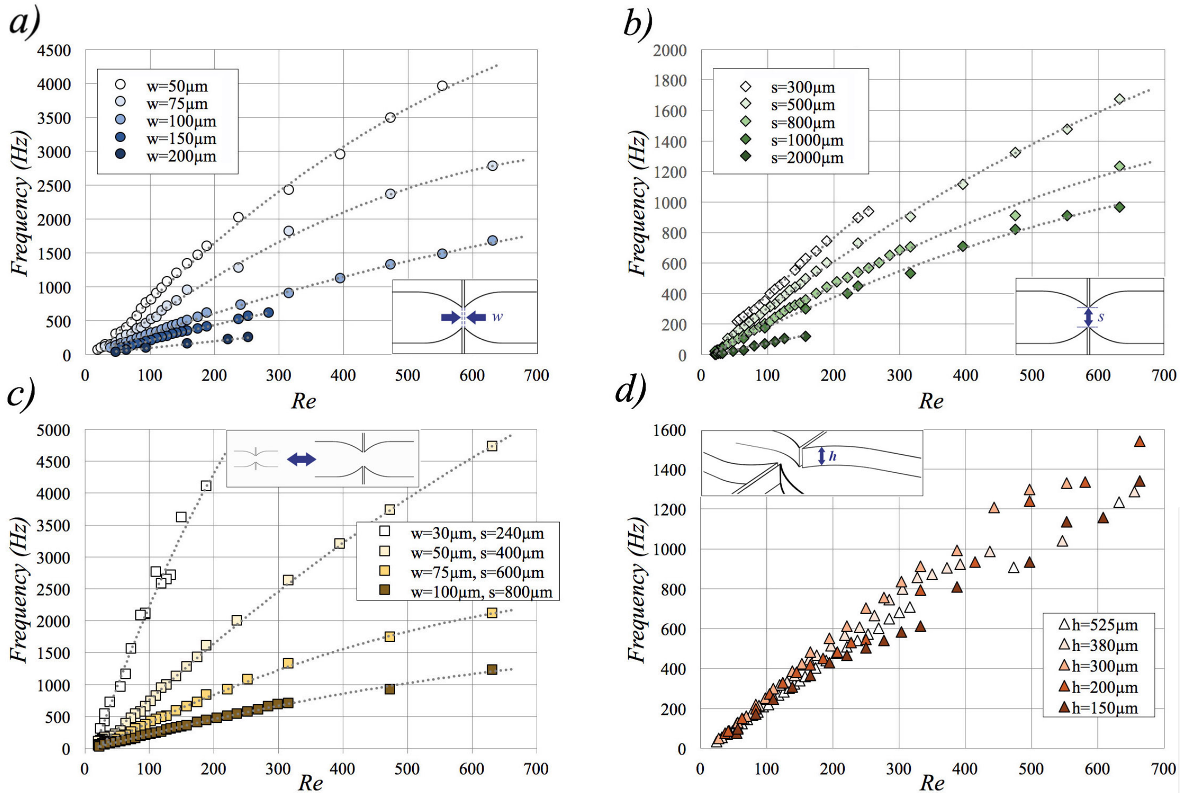

Figure 6. Evolution of the self-oscillation frequency with Re, when geometric parameters are changed. a) The width of the jets is changed, all other geometric dimensions being constant ($h = 525\,\mu m$, $s = 500\,\mu m$, $L = 2000\,\mu m$). b) The distance between of the jets is changed, all other geometric dimensions being constant ($h = 525\,\mu m$, $w = 100\,\mu m$, $L = 2000\,\mu m$). c) The overall dimension of the oscillator is changed, with the ratio s/w being constant. The height of the devices is $h = 525\,\mu m$. d) The height h of the devices is changed, all other dimensions being equal ($w = 100\,\mu m$, $s = 800\,\mu m$, $L = 2000\,\mu m$). The dotted lines are drawn only to guide the eye.

jets changes, all other geometric dimension being identical across all devices ($h = 525\,\mu m$, $w = 100\,\mu m$, $L = 2000\,\mu m$). For a chosen distance between the impinging jets, the oscillation frequency increases with Re, and at a chosen value of Re, the oscillation frequency increases when the distance between jets decreases. When the distance between the jets increases, the threshold at which the oscillations start, occurs for smaller values of Re. Oscillator geometries of identical design but having a distance of only $200\,\mu m$ between the jets were also tested, but oscillations could not be observed with these devices. For a distance between the jets of $300\,\mu m$, stable oscillations occur only in a limited range of Re, and stop when Re

is larger than 250. When the distance between the jets is 2000 μm, which corresponds to the full width of the exit channel, stable oscillations where the impinging jets alternate are also occurring in a limited range of Re. In this case, $s = L$, as it was the case in the experiments presented in Fig. 2 and 4, and the reduced range of oscillation frequencies observed is related to the absence of extension in the output channel as discussed previously.
Fig. 6-c shows the evolution of the oscillation frequency with Re, when the overall dimension of the oscillator is changed, while keeping constant the ratio s/w. The height of all oscillators studied here is 525 μm. For all oscillators measured, the threshold where oscillations started was close to $Re = 22$, and oscillations could be observed when increasing Re, until the maximal flow rate the syringe pumps could provide was reached. When the oscillators dimensions are smaller, the frequency of the oscillations are higher for any given value of Re. Impinging jets having the same ratio s/w but an inlet channel of only 10 μm in width were also fabricated. These were very sensitive to the presence of dust particles in the water flows, but oscillations were observed when using filtered dye solutions. An accurate value of the oscillation frequency could not be measured, as the oscillations were very fast and a high-magnification microscope objective was used, which strongly limited the amount of light available to image the phenomenon with the high-speed camera.
Fig. 6-d shows the evolution of the oscillation frequency with the height of the fabricated structures. When performing measurements, oscillations were observed over a large range of Re for all values of the height of the oscillators tested. However, for the oscillators of height smaller than 300 μm, the impinging jets showed irregular oscillations frequencies, in particular for values of Re larger than 200. In this case, the jet oscillations superimposed with a large oscillation of the entire exit channel that occurs at a much lower frequency than the jet oscillations.

Fig. 7 shows the evolution of the parameter obtained by multiplying the frequency f and the distance between the jets s versus the average velocity U of the liquid flow at the nozzles for all measurements previously presented in Fig. 6. A linear dependence is observed, indicating the importance of the spacing between the jets in the self-oscillation phenomenon. The linear fit of all data points presented in this figure has a slope of 1/6, which is consistent with the measurements made by Denshikov *et al.* on large scale facing jets in turbulent flow conditions (Denshikov presented an empirical formula that translates to $1/f = 6s/U$, when using the notations of the present paper) [29]. Without pretending more, as a matter of

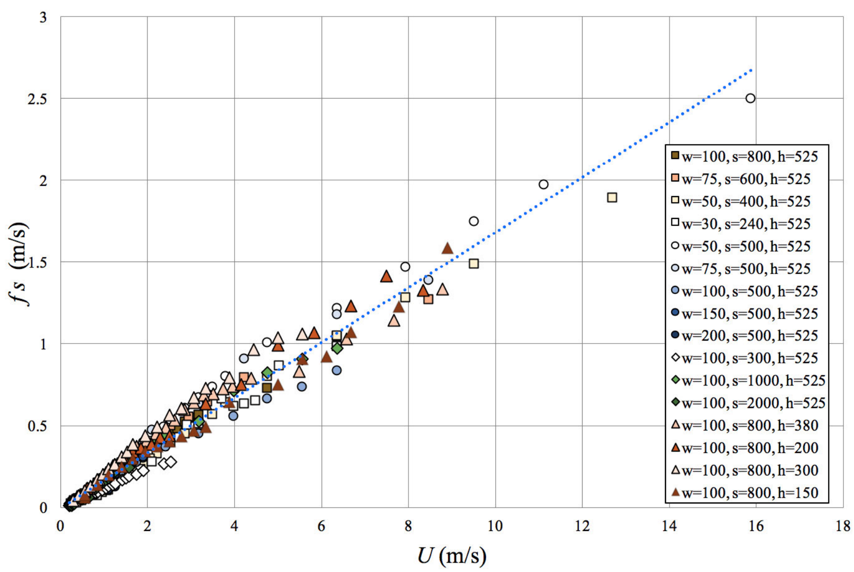

Figure 7. The frequency multiplied by the spacing between the jets $f \cdot s$ versus the average speed of the jets, U, for all the data presented in Fig. 6. The blue dotted line is a linear fit of all data.

fact, the Strouhal number pertaining to many self-sustained oscillator flows (the wake of a cylinder for instance) is often found in the range 0.1-0.2.

D. Second oscillation mode

In the case of oscillator geometries based on large straight output channels (such as the oscillator of dimensions $w = 100\,\mu m$, $s = 2000\,\mu m$, $L = 2000\,\mu m$, $h = 525\,\mu m$), two oscillation modes can be observed. The first oscillation mode (Fig. 8-a) is similar to the oscillations presented previously, the jets first bifurcate in opposite directions and later come back towards one another, collide and switch sides. This first oscillation mode occurs for low values of the Reynolds number (in the case of the oscillator presented in Fig. 8-a, for Re between 20 and 65). For large values of the Reynolds number, a second mode of regular oscillations was observed (Fig. 8-b), where the jets do not switch sides but bounce against each other at regular time intervals, each bounce resulting in a complex rotating flow motion at the center of the channel (in the case of the oscillator presented in Fig. 8-b, this second mode is seen for Re between 65 and 160). This second oscillation mode has been observed for straight-channel oscillators where the ratio s/w is larger than 20, and seems to become

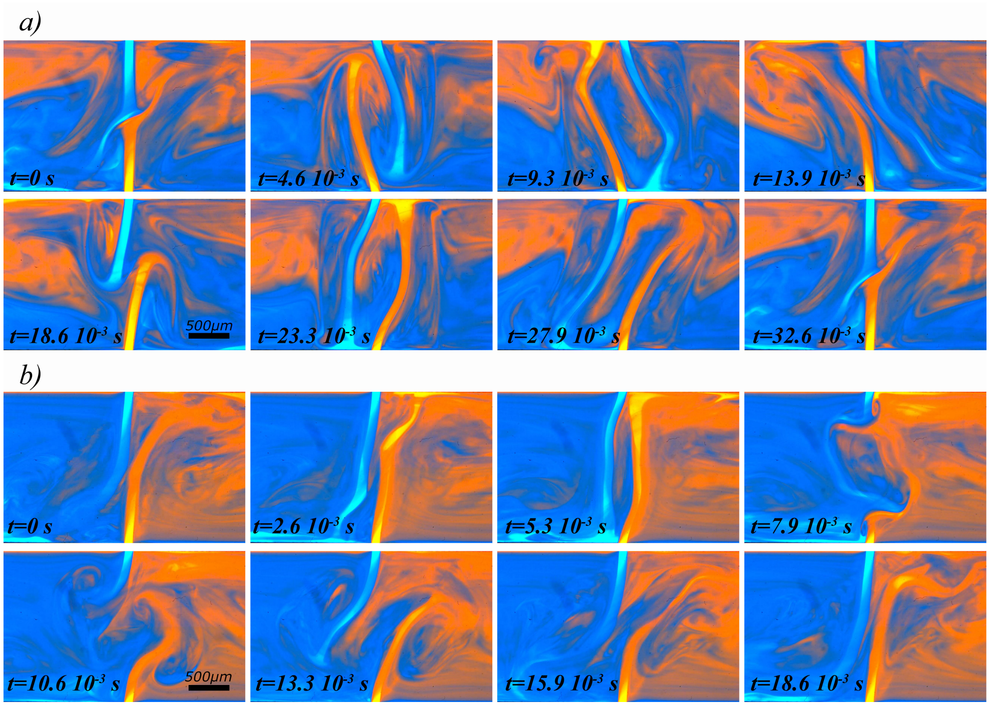

Figure 8. Evolution of the fluid flow during one oscillation. Experimental dyes concentration fields obtained for an oscillator of dimensions $w = 100\,\mu m$, $s = 2000\,\mu m$, $L = 2000\,\mu m$, $h = 525\,\mu m$. Images are taken at regular time intervals (from left to right, top to bottom). *a*) $Re = 47$, $F = 23\,Hz$, the liquid jets collide and switch sides at each oscillation. *b*) $Re = 79$, $F = 30\,Hz$, the jets do not switch sides but bounce against each other regularly, each bounce resulting in a rotating flow motion in the center of the channel (see movie S4 in Supplemental Material [32]).

dominant for straight-channel oscillators with even larger s/w ratios.

IV. DIRECT NUMERICAL SIMULATIONS

A. Governing equations

The fluid motion inside the microfluidic oscillator domain, denoted by Ω, is governed by the unsteady incompressible three-dimensional Navier-Stokes equations,

$$\nabla \cdot \mathbf{u} = 0 \quad \text{on } \Omega, \tag{2}$$

$$\frac{\partial \mathbf{u}}{\partial t} + \mathbf{u} \cdot \nabla \mathbf{u} = \nabla p + \frac{1}{Re} \nabla \cdot \boldsymbol{\tau} \quad \text{on } \Omega, \tag{3}$$

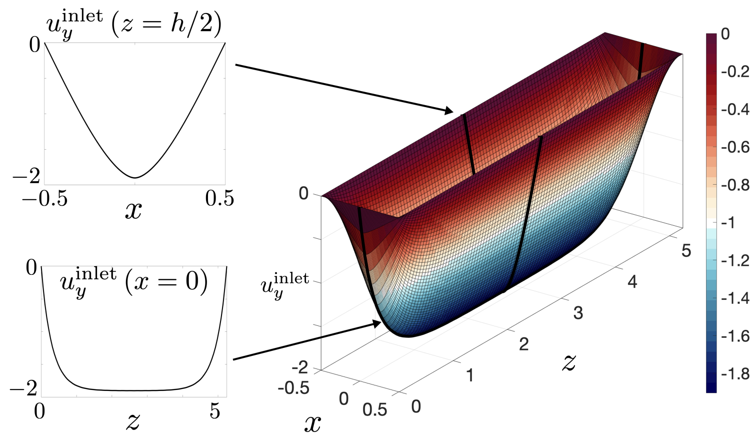

Figure 9. Fully developed velocity profile, having unitary mean velocity, in a rectangular microchannel, imposed as boundary condition at the inlets. Non-dimensional values of the x-coordinate between -0.5 and 0.5 correspond to a $100\,\mu m$ inlet channel width w, while values of the z-coordinate between 0 to 5.25 corresponds to a microfluidic oscillator of $525\,\mu m$ in height h.

where $\mathbf{u} = \{u_x, u_y, u_z\}^T$ is the velocity flow field, Re the Reynolds number and $\boldsymbol{\tau} = \left[\nabla\mathbf{u} + \nabla^T\mathbf{u}\right]$ the viscous stress tensor. Eqs. (2)–(3) are made non-dimensional by scaling lengths, velocity components and time respectively with the inlet channel width w, the average fluid velocity at the inlets U, and the convective time w/U, respectively. The Reynolds number is thus defined by Eq. (1), while the pressure is scaled by ρU^2.

In addition to the fluid governing equations, we introduce a further advection-diffusion equation fully decoupled from Eqs. (2)–(3) and describing the dynamics of a passive scalar, Φ,

$$\frac{\partial \Phi}{\partial t} + \mathbf{u}\cdot\nabla\Phi = \frac{1}{Pe}\Delta\Phi, \tag{4}$$

(analogous to the temperature equation) which allows us to reproduce the two dyes injected during the experiments. The Péclet number, Pe, appearing in Eq. (4) has been set to $Pe = 100$ in order to ensure a good numerical stability and get a satisfactory flow visualization at the same time for all the particular geometries and control parameters, i.e. Re, considered. The oscillator cavity is assumed to be perfectly rigid, therefore a no-slip boundary condition for the velocity field, $\mathbf{u}|_{\partial\Omega} = \mathbf{0}$, is enforced at the solid boundary domain, denoted by $\partial\Omega$. At the outlets, a traction-free boundary condition is imposed, $\mathbf{t}_n = \left[-p\mathbf{I} + \frac{1}{Re}\left(\nabla\mathbf{u} + \nabla^T\mathbf{u}\right)\right]$, where $\mathbf{I}$ denotes the identity matrix; in general, this boundary condition is used to model

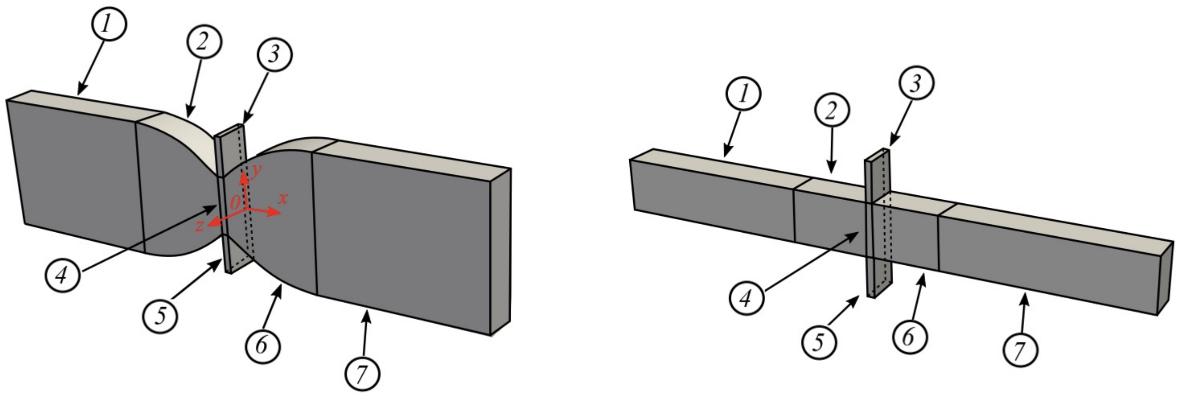

Figure 10. Domain's sub-division in macro boxes labeled by circled numbers: in presence of expansion channel, the mesh is stretched and remapped according to the prescribed radius of curvature.

flow exits where details of the flow velocity and pressure are not known *a priori*; it is an appropriate boundary condition here, where the exit flow is close to be fully developed. At the inlets, the experimental constant flow rate is reproduced imposing the typical velocity profile present in rectangular micro-channels (see the analytical solution described in [33]), shown in Fig. 9. The length of the inlets ducts is such that assumed to be long enough for a fully developed flow is ensured.

Concerning the passive scalar equation, Dirichlet boundary conditions are imposed at the two inlets ($\Phi = 0, 1$) to reproduce the injection of dyes, while outflow conditions are set at the outlets; no-flux is allowed through the solid walls.

B. Numerical procedure for DNS

The opens-source code Nek5000 [34] has been used to perform the direct numerical simulation. The spatial discretization is based on the spectral element method (SEM). The three-dimensional geometry is divided in 7 macro boxes (as indicated in Fig. 10); each macro box is then characterized by an imposed number of hexahedral elements, along the three Cartesian coordinates x, y and z , within which, the solution is represented in terms of N-th order Lagrange polynomials interpolants, based on tensor product arrays of Gauss-Lobatto-Legendre (GLL) quadrature point in each spectral element; the common algebraic P_N/P_{N-2} scheme is implemented, with N fixed to 7 for velocity and 5 for pressure. In all cases numerically examined, the overall length of the full oscillator structure in the x-direction, as well as the inlet ducts lengths in the y-direction (box 3 and 5), are kept constant and equal to $80w$ and $6w$, respectively. The inlet channel lengths are fixed to $10w$ (value in the range where experimental tests showed insensitivity of the oscillation frequency with Re to the inlet channel length). All the others characteristic sizes are changed in accordance to the definition of w, h, s and L associated with the considered microfluidic oscillator geometry. Macro box 2 and 6, originally rectangular, are stretched or not depending on whether or not the expansion channel is present ($s \neq L$ or $s = L$). The domain is thus discretized with a structured multiblock grid consisting of, depending on the geometry analyzed, 32320 (if $s = 8w$) or 58880 (if $s = 20w$) spectral elements. The time-integration is handled with the semi-implicit method IM/EX, already implemented in Nek5000; the linear terms in Eqs.(2)-(3) are treated implicitly adopting a third order backward differentiation formula(BDF3), whereas the advective nonlinear term in Eq.(3) is estimated using a third order explicit extrapolation formula (EXT3). The semi-implicit scheme introduces restriction on the time step [35], therefore an adaptive time-step is set to guarantee the Courant-Friedrichs-Lewy (CFL) constraint.

V. COMPARISON BETWEEN EXPERIMENTS AND DNS

A. Dyes, concentration fields

Fig. 11, 12 and 13 show the evolution of the dyes concentration field during one oscillation, with each figure corresponding to the case of an oscillator of specific geometry and a given flow condition. Fig. 11 refers to an oscillator geometry made of a simple straight channel without expansion, similar to the one described in Fig. 2 ($w = 100\,\mu m$, $s = 800\,\mu m$, $L = 800\,\mu m$, $h = 525\,\mu m$ and $Re = 60$).

Fig. 12 shows an oscillator with an expansion in the output channel, similar to the one presented in Fig. 3 (oscillator dimensions are $w = 100\,\mu m$, $s = 800\,\mu m$, $L = 2000\,\mu m$, $h = 525\,\mu m$ and $Re = 60$). Fig. 13 corresponds to an oscillator geometry made of a simple straight channel having a large output width (oscillator dimensions are $w = 100\,\mu m$, $s = 2000\,\mu m$, $L = 2000\,\mu m$, $h = 525\,\mu m$ and $Re = 50$). In all three figures, images are taken at regular time intervals during one oscillation and compare the measured and simulated concentration fields. The images obtained experimentally show a depth averaged

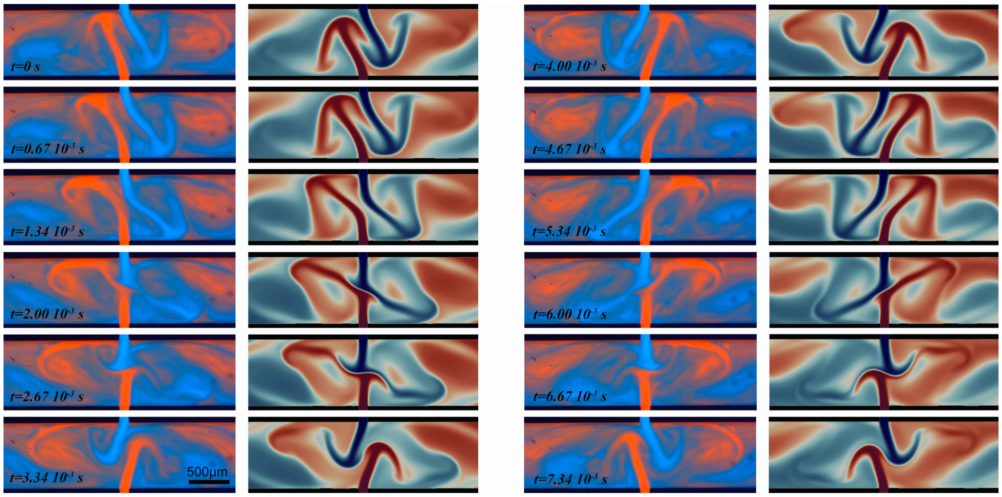

Figure 11. Evolution of the fluid flow with time during one oscillation. Comparison of experimental and simulated dye concentration fields in the case of an oscillator of dimensions $w = 100\,\mu m$, $s = 800\,\mu m$, $L = 800\,\mu m$, $h = 525\,\mu m$ at $Re = 60$. The images are taken at regular time intervals (from top to bottom, left to right) (see movie S5 in Supplemental Material [32]).

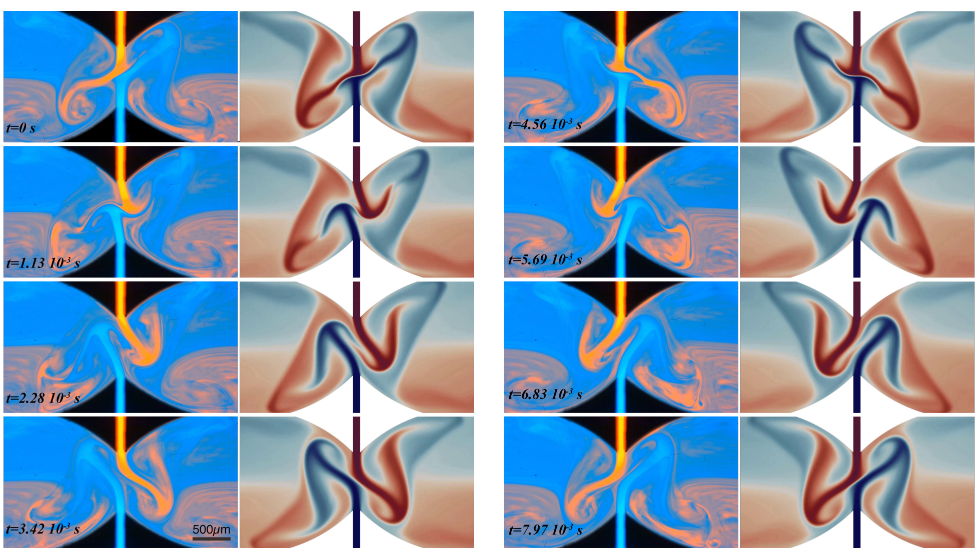

Figure 12. Comparison of experimental and simulated dye concentration fields in the case of an oscillator of dimensions $w = 100\,\mu m$, $s = 800\,\mu m$, $L = 2000\,\mu m$, $h = 525\,\mu m$ at $Re = 60$. The images are taken at regular time intervals (from top to bottom, left to right) (see movie S6 in Supplemental Material [32]).

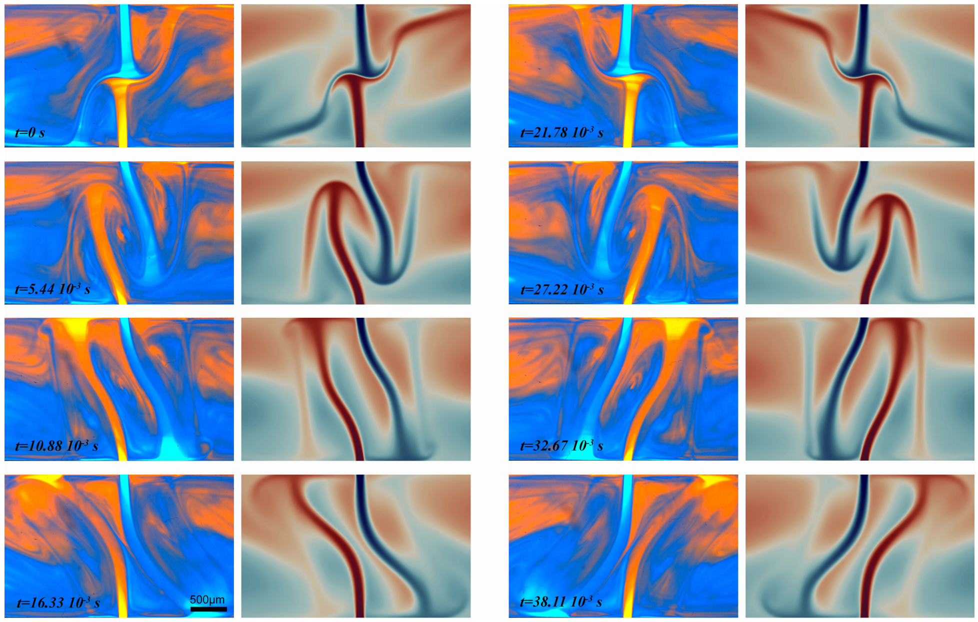

Figure 13. Comparison of experimental and simulated dye concentration fields in the case of an oscillator of dimensions $w = 100\,\mu m$, $s = 2000\,\mu m$, $L = 2000\,\mu m$, $h = 525\,\mu m$ at $Re = 50$. The images are taken at regular time intervals (from top to bottom, left to right) (see movie S7 in Supplemental Material [32]).

concentration, as they integrate the light passing through the full height of the microchannels, whereas in the case of the simulation, the images show the concentration field in the x-y plane of median height ($212.5\,\mu m$ from the bottom of the microchannel). All simulations have been run starting from zero initial conditions. In all cases, there is a good agreement between the experimental and simulated dyes concentration fields, with the main flow features being similar for each chosen time step. The smaller features differ however between experiments and simulations, which may be related to the fact that the experimental images result from the integration of the light crossing the full height of the microstructure or to a non-optimal calibration of the Péclet number in the simulation.

B. Non-dimensional frequency

In addition to the dyes concentration fields, simulations also provide the non-dimensional frequency of the self-oscillation phenomenon at the chosen value of the Reynolds number, expressed by the Strouhal number $St = f\frac{w}{U}$. Fig. 14-*a*-*b* and *c* compare the experimental and

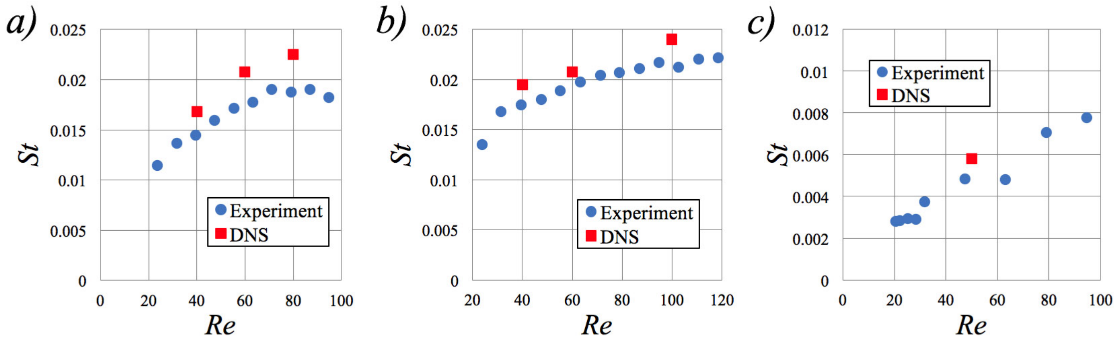

Figure 14. Experimental and numerical non-dimensional oscillation frequency expressed by the Strouhal number $St = f\frac{w}{U}$ versus the Reynolds number Re. a), b) and c) correspond to Fig. 11, Fig. 12 and Fig. 13, respectively.

simulated values of St, in the case of the three oscillator geometries presented in Fig. 11, 12 and 13 respectively. The DNS slightly over-estimates the value of the oscillation frequency in all cases, however, the results of simulation are generally close to the measurements. This little overestimation can be partially attributed to the numerical inlet velocity profile, which may not exactly represent the experimental profile. In the case of the oscillator with straight output channels (Fig. 14-a), a deviation between simulations and experiments can be seen at large values of Re. This is close to the conditions described in Fig. 2, where the jets stop to alternate regularly and which we linked to the absence of the expansion in the output channel. In such conditions, the liquid jets strongly interact with the walls, as the simulated pressure field shows in Fig. 15. This jet-wall interaction increases with increasing values of Re, and at some point, interferes with the increase of the self-oscillation frequency, inducing the stop of the alternating motion of the jets observed experimentally. Apparently, the DNS correctly predicts the interaction of the jets with the walls, but the ideal conditions described by the simulation do not correctly account for the change of frequency occurring experimentally close to this change of flow regime, probably induced by the small imperfections of the manufactured components and of the dust particles present in the liquid flows. Note that this interaction of the jets with the walls does not occur in the case of oscillator geometries presenting an expansion in the output channel, as the jets motion follows the wall curvature. This could explains the much wider range of stable oscillations, $[Re_c, Re_{irr}]$, observed experimentally for such oscillator geometries.

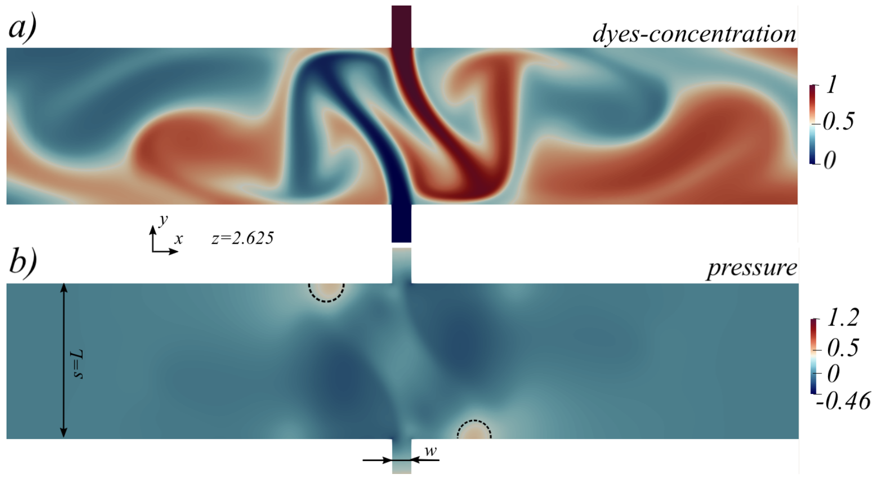

Figure 15. a) Simulated dye concentration and b) pressure fields (slice x-y at $z = 2.625$), showing the jet interaction with the walls occurring in the case of oscillators having straight output channels ($w = 100\,\mu m$, $s = L = 800\,\mu m$, $h = 525\,\mu m$ at $Re = 60$). The maximum pressure is always encountered at the domain's center, where the two jets face each other. Nevertheless, in b) we observe two regions of high pressure (highlighted in dashed black lines) occurring when the jets interact with the solid walls and whose intensity increases as Re in increased.

VI. VELOCITY FIELD DESCRIPTION

In §V we provided several comparison between experimental results and numerical simulations in terms dyes concentrations fields and oscillation frequency, showing a good agreement, which allows us to reasonably use the numerical results in order to investigate the various velocity fields more in depth.

A. Steady configuration

As mentioned, all the simulations were started from zero initial conditions, with the inlet velocity profile of Fig. 9 constantly enforced at the two inlets. After a first transient required for the flow to invade the whole cavity domain, a stationary configuration firstly manifests itself. This steady flow is always observed. If the Reynolds number is higher than the instability threshold, it is observed for a certain time interval, after which the self-sustained oscillations start with the periodic flow configuration discussed in the previous sections. On the contrary, if Re is set below this threshold, then the flow remains stationary indefinitely.

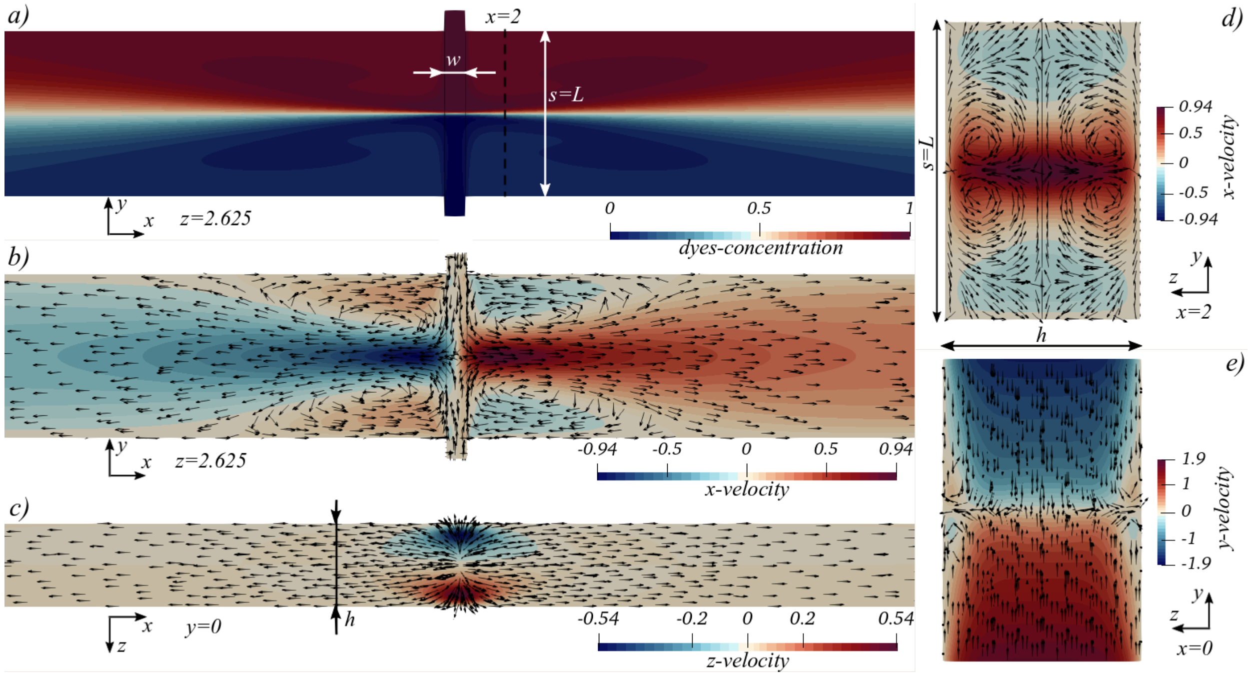

Figure 16. a) Dyes concentration and b, c, d, e) stationary velocity field numerically observed before the self-sustained oscillation start in the case of the microfluidic oscillator of Fig. 11, $w = 100\,\mu m$, $s = 800\,\mu m$, $L = 800\,\mu m$, $h = 525\,\mu m$ at $Re = 32$. b) Filled 2D contour plot for u_x and black arrow for the in-plane velocity vector, $\{u_x, u_y\}$. c) Filled 2D contour plot for u_z and black arrow for the in-plane velocity vector, $\{u_x, u_z\}$. d) Filled 2D contour plot of the out of plane velocity u_x and black arrow for the in-plane velocity vector, $\{u_y, u_z\}$. Slices size are not to scale. Arrows provides a qualitative representation only. e) Filled 2D contour plot for u_y and black arrow for the in-plane velocity vector, $\{u_y, u_z\}$. Slice represented in b), c) and e) correspond to the three main plane of symmetry (indicated in figure).

This stationary configuration is shown in fig. 16 for the microfluidic oscillator based on straight output channels ($w = 100\,\mu m$, $s = 800\,\mu m$, $L = 800\,\mu m$, $h = 525\,\mu m$ at $Re = 32$).

From Fig. 16-b we observe two large recirculation regions close to the channel inlets and resulting from the presence of walls, where a no-slip boundary conditions is enforced. The three-dimensional shape of these recirculation regions can be clearly seen in Fig. 16-d. Heading towards the channel outlets, the flow approaches a fully developed flow having substantially null u_y and u_z velocity components. From Fig. 16-c and d we also note two regions of vortical motion in the collision region of the jets; this is due to the constant

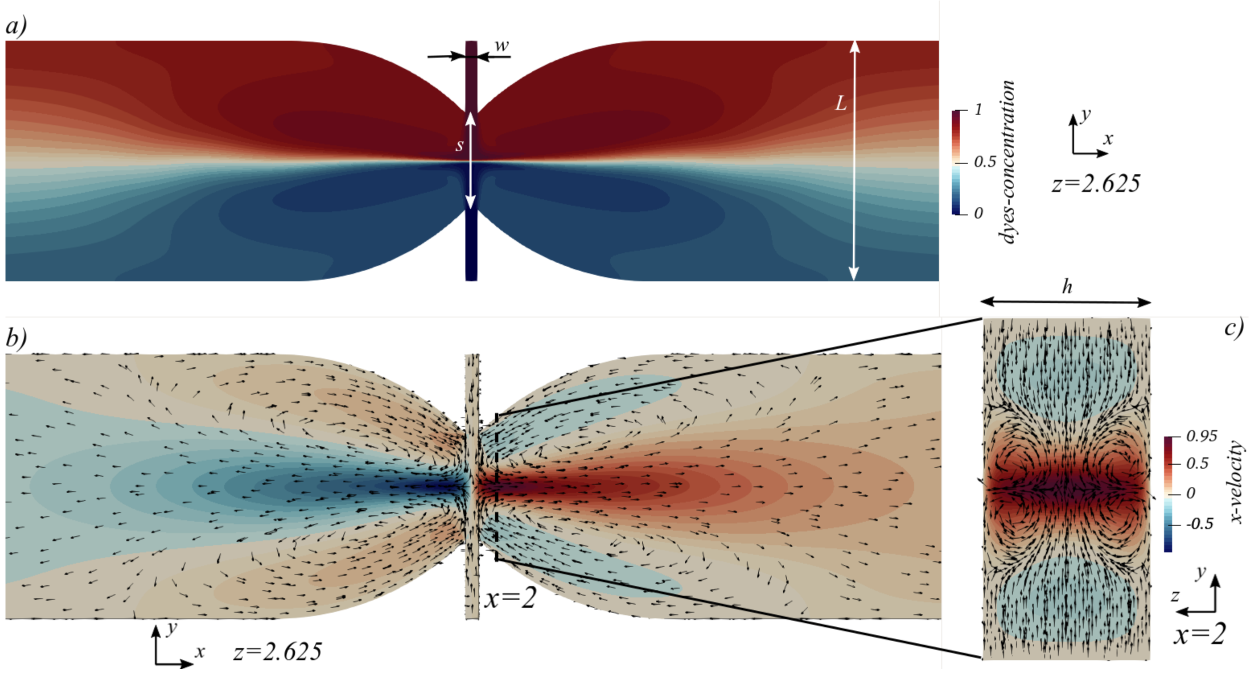

Figure 17. a) Dyes concentration and b, c, d, e) stationary velocity field numerically observed before the self-sustained oscillation start in the case of the microfluidic oscillator of Fig. 12, $w = 100\,\mu m$, $s = 800\,\mu m$, $L = 2000\,\mu m$, $h = 525\,\mu m$ at $Re = 30$. b) Filled 2D contour plot for u_x and black arrow for the in-plane velocity vector, $\{u_x, u_y\}$. c) Filled 2D contour plot of the out of plane velocity u_x and black arrow for the in-plane velocity vector, $\{u_y, u_z\}$. Slices size are not to scale. Arrow provides a qualitative representation only.

pressure that the two jets exert against each other; indeed, the pressure field (not represented in Fig. 16) is characterized by a high pressure region spatially located where the jets collide. As the jets face each other, the fluid tends to escape in all directions, thus part of the fluid escaping along the z-direction meets the lateral solid walls at $z = 0$ and $z = h$, which push back the fluid, leading to this vortical motion.

Fig. 17 is the equivalent of Fig. 16, but in the case of the oscillator with an expansion in the output channel ($w = 100\,\mu m$, $s = 800\,\mu m$, $L = 2000\,\mu m$, $h = 525\,\mu m$ and at $Re = 30$).

This configuration is similar to the one presented in Fig. 16 with respect to the value of Re and the spacing s. Now the presence of an expansion region in the output channel leads to the formation of two much more elongated recirculation regions along the x-direction, which follow the curvature of the cavity (Fig. 17-b). Because of the cavity's curvature, the vertical velocity within these recirculation regions is larger when compared to Fig. 16-b. Planes $x-z$ at $y=0$ for u_z and $y-z$ at $x=0$ for u_y are not shown here since they are qualitatively and quantitatively close to those of Fig. 16.

B. Self-oscillating configuration

When the Reynolds number is increased above the instability threshold, i.e. $Re > 23$ for the microfluidic oscillator of Fig. 16, the two jets start to oscillate regularly for a wide range of Re. As already mentioned in §III, the jets regularly collide against each other and switch sides in a periodic motion. At each collision, a pair of three-dimensional vortices is emitted and advected towards the channel outlets, as can be observed in Fig. 18-b and c.

The two stable vortical regions represented in Fig. 16 and Fig. 17 are now alternately pushed up and down owing to the continuous switch of side of the oscillating jets, as show in Fig. 18-b and d. A qualitatively similar flow evolution in time is recognized for the microfluidic oscillator with the expansion channel, meaning the physical mechanism which breaks the symmetry of the stationary configuration and leads to the unsteady periodic motion is the same, while the expansion channel only contributes to stabilize the regular oscillations up to a much higher Re.

C. Perturbation fields

As mentioned in §VI A, the steady configuration, which is linearly stable for $Re < Re_c$, is transiently observed even for $Re > Re_c$, before the amplitude of the oscillating perturbation, which grows exponentially, becomes large enough for the self-sustained oscillations to settle into a limit cycle. In the spirit of the linear global stability analysis, the total velocity and pressure fields in the vicinity of the threshold can be decomposed as the sum of a steady base flow and a time-dependent perturbation field:

$$\mathbf{u}\left(x,y,z,t\right) = \mathbf{u}_{bf}\left(x,y,z\right) + \mathbf{u}_{p}\left(x,y,z,t\right), \tag{5}$$

$$p\left(x,y,z,t\right) = p_{bf}\left(x,y,z\right) + p_{p}\left(x,y,z,t\right). \tag{6}$$

The total velocity field, $\mathbf{u}$, and pressure field, p, extracted from the DNS can thus be used to separate the corresponding perturbation fields, $\mathbf{u}_p$ and p_p, from the base-flow fields, $\mathbf{u}_{bf}$ and p_{bf}, and highlight where the origin of the regular oscillations is located. Let us consider, i.e., the microfluidic geometry of Fig. 16 and 18. A series of numerical simulations, starting

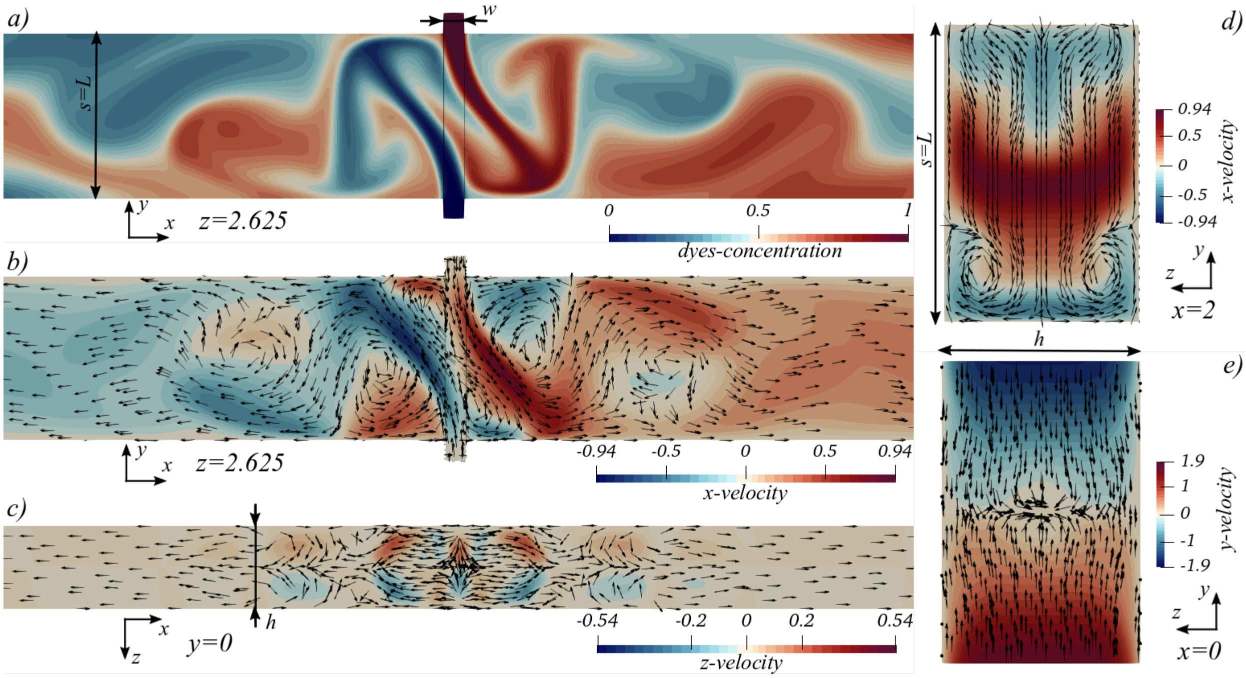

Figure 18. Snapshot of a) dyes concentration and b, c, d, e) unsteady velocity field numerically observed once the self-sustained oscillations reached the limit cycle in the case of the microfluidic oscillator of Fig. 11, $w = 100\,\mu m$, $s = 800\,\mu m$, $L = 800\,\mu m$, $h = 525\,\mu m$ at $Re = 60$. b) Filled 2D contour plot for u_x and black arrow for the in-plane velocity vector, $\{u_x, u_y\}$. c) Filled 2D contour plot for u_z and black arrow for the in-plane velocity vector, $\{u_x, u_z\}$. d) Filled 2D contour plot of the out of plane velocity u_x and black arrow for the in-plane velocity vector, $\{u_y, u_z\}$. e) Filled 2D contour plot for u_y and black arrow for the in-plane velocity vector, $\{u_y, u_z\}$. Slice represented in b), c) and e) correspond to the three main plane of symmetry (indicated in figure). Slices size are not to scale. Arrows provides a qualitative representation only.

from zero initial conditions, were performed in the range $Re = 18 - 25$ (the threshold, Re_c, for the case here considered is approximatively 23). Fig. 19 -a) and b) show the value of the of the x- an y-velocity components at the coordinate $(x, y, z) = (3, 0, 2.625)$. Since the oscillating flow configuration breaks the antisymmetry of the y-velocity component with respect to the x-z plane in $y = 0$, the y-component is then monitored (see Fig. 19 -b)) in time to establish at which Re and time-instant the oscillations start to be visible.

As shown in Fig. 19 -b), the flow does not exhibit any oscillations below Re_c, where only the linearly stable base-flow is observed. For $Re = 25 > Re_c$, oscillations start to grow

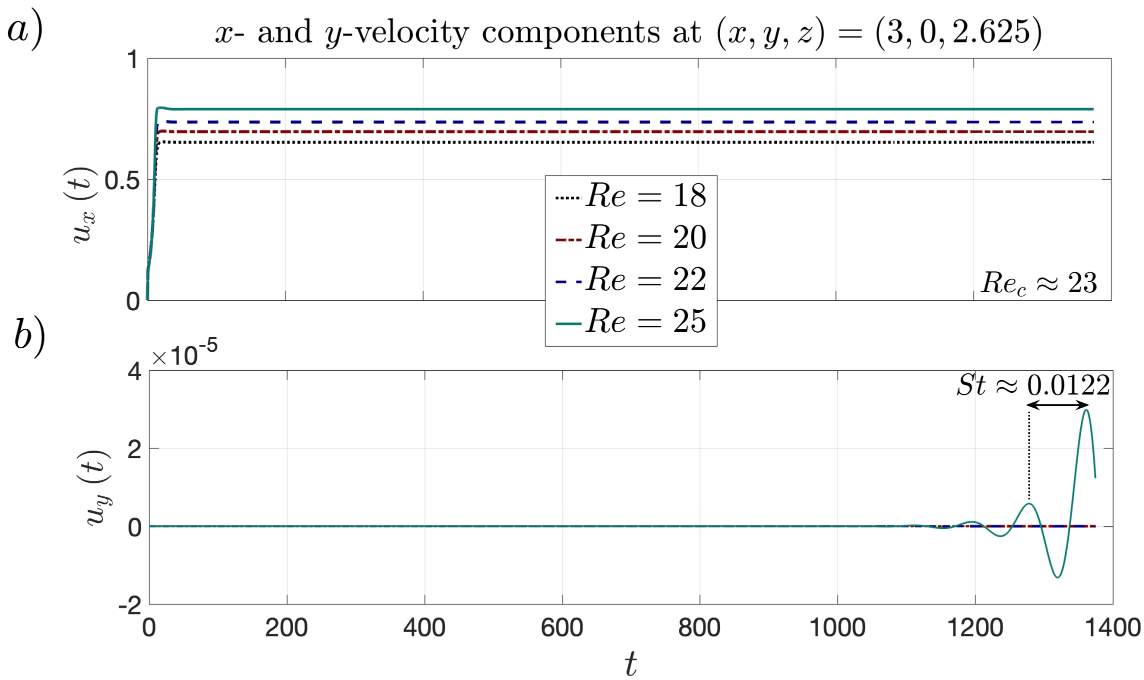

Figure 19. a) Horizontal, u_x, and b) vertical, u_y, velocity components at $(x, y, z) = (3, 0, 2.625)$. The plane $x - y$ at $z = h/2$ is a plane of antisymmetry for the perpendicular velocity component, $u_z|_{z=h/2} = 0$. b) The antisymmetry of u_y with respect to the plane $x - z$ at $y = 0$ is broken for $Re = 25$, which is slightly higher than the threshold value, $Re_c \approx 23$. Note that the resulting Strouhal number agrees well with the experimental one presented in Fig. 14 -a), even if the limit cycle has not been reached yet.

from zero with a very small growth rate, given the vicinity to the marginal stability. In such conditions, the stationary base-flow velocity and pressure fields, $\mathbf{u}_{bf}$ and p_{bf}, can be identified where the perturbation is still very small, i.e., at $t = 400$, where the order of magnitude of the perturbation is lower than 10^{-10}. Subtracting this base-flow from the total flow, i.e. at $t = 1375$ in Fig. 19, allows to isolate the growing perturbation, as presented in Fig. 20.

The analysis of the perturbation velocity fields allows to locate the origin of the oscillations in the central region, where the jets collide and curve towards the output channels. Well defined counter-rotating vortical structures, whose extension in the z-direction cover the entire channel height h and which are separated by a wavelength λ suggesting a correlation with the distance separating the inlets, s, are generated and advected downstream (left

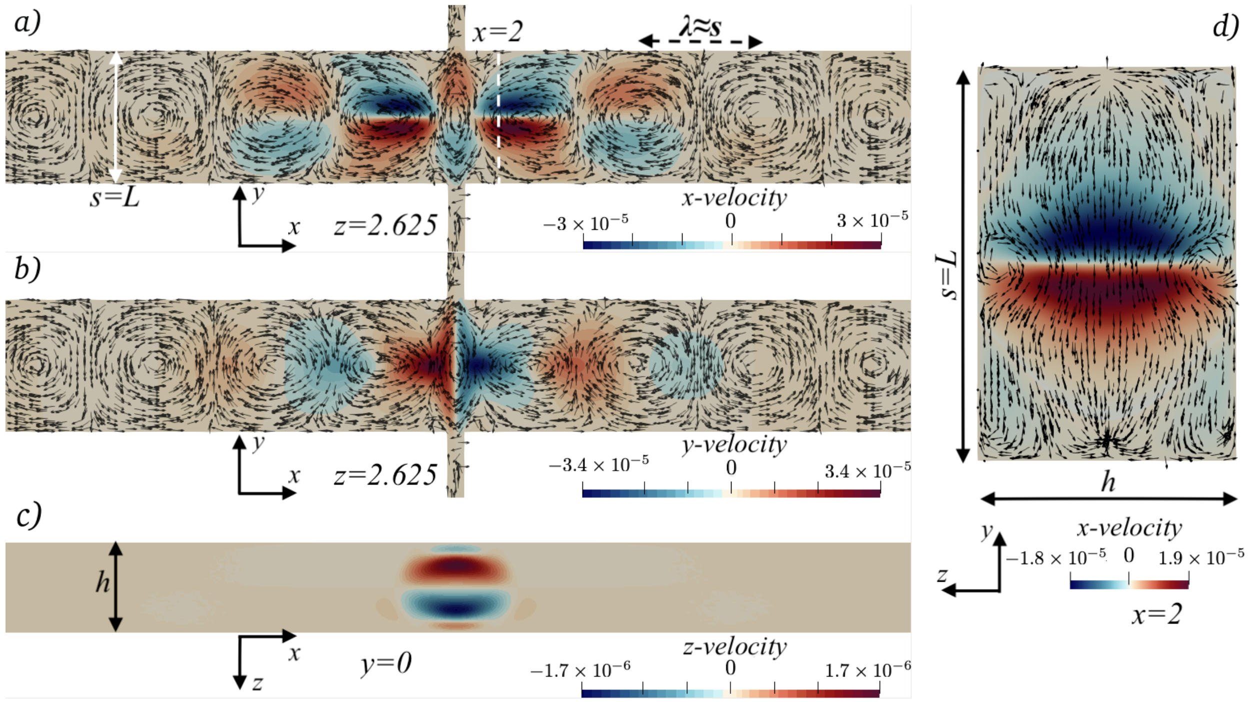

Figure 20. *a*)-*b*) Filled contours of the x and y perturbation velocity components extracted for $t = 1375$ in Fig. 19-*b*) for the microfluidic oscillator with $w = 100\,\mu m$, $s = 800\,\mu m$, $L = 800\,\mu m$, $h = 525\,\mu m$ at $Re = 25$. The black arrows represent the orientation of the in-plane velocity vector, $\{u_x, u_y\}$. *c*) Filled contours for u_z in the $x - z$ slice at $y = 0$. Slices size are not to scale. Arrows provides a qualitative representation only. *d*) Filled contours of the out of plane velocity u_x and black arrows for the in-plane velocity vector $\{u_y, u_z\}$ in the $y - z$ slice at $x = 0$.

and right) by the base-flow (see Fig. 20-*a*) and *b*)). The z-velocity component is significantly smaller than the other two components in the central region and negligible in the rest of the domain, as shown in Fig. 20-*c*) and *d*).

D. Discussion

Despite the insight brought by the numerical simulations to visualize the total velocity and pressure fields, and the perturbation fields, no physical mechanism could be precisely identified, from which these self-sustained oscillations would originate. Several plausible candidates can be tentatively identified. Hyperbolic stagnation points and lines are well known to be unstable [36, 37], although they often lead to static bifurcations [10]. The existence of recirculation regions is quite similar to sudden expansion flows which are also known to become statically unstable [38]. But these recirculation regions also form an intense shear layer, which could possibly become the source of a Kelvin-Helmholtz instability. Indeed, the structure of the perturbation velocity field in the left and right channels shown in Fig. 20 is typical of sinuous shear instabilities. In order to translate into a global instability, this shear layer instability would either need to be of absolute nature, possibly because of the presence of near-by walls, known to enhance absolute instability in confined shear flows [39–42]. Even if this shear layer instability were to be convective, other feedback mechanisms, as the ones investigated in Villermaux [43, 44] could also ensure the global, sefl-sustained nature of the observed oscillations. In order to get further insight, an exhaustive stability analysis of the present flow needs to be conducted, which could locate the wavemaker region and clearly indentify the governing instability mechanisms at stake.

VII. COMMENTS AND CONCLUSIONS

Pulsatile liquid flows showing a self-oscillation behavior were studied at the microscale. Experimentally, oscillating water jets were generated in microfabricated silicon cavities, from steady and equal inlet flows and without external stimuli. They were colored imaged using a microscope and a high-speed camera. The oscillators we described here can be categorized as based on jet interactions: Two facing jets first bifurcate in opposite directions and later come back towards one another, collide and switch sides, with a very regular temporal periodicity.

Direct numerical simulations were performed to solve the unsteady incompressible three-dimensional Navier-Stokes equations in the studied geometries, using a spectral element method. The Nek5000 was used to perform the simulation. Experiments and simulations show a good agreement for all studied oscillators, for both the dye concentration fields and the non-dimensional oscillation frequency.

The self-oscillation phenomenon starts at a threshold, in terms of Reynolds number, that depends on the geometrical parameters of the oscillator cavity. Threshold values close to $Re = 20$ were observed for many of the studied geometries.

When the oscillator is based on simple straight crossing channels, the self-oscillation phenomenon can be observed for a limited range of values of the Reynolds number, since when Re exceeds a second threshold Re_{irr}, the flows stop to switch sides regularly and periodicity is lost. The corresponding simulated pressure field evolution shows that the jets strongly interact with the output channel walls in this case, which induces this change of flow regime. When the output channel is no longer a simple straight channel but is supplemented by an expansion, this interaction with the walls is no longer occurring, as the jets motion follows the wall curvature. This leads to a much wider range of stable oscillations. Experimentally, the impinging jets were observed to switch sides regularly until the pumps used could not deliver higher flow rates and stalled (for $Re = 630$).

The evolution of the self-oscillation frequency was studied when the main geometric parameters of the oscillator cavity were changed. A linear dependence between the average flow velocity and the parameter obtained by multiplying the oscillation frequency and the distance between the jets was observed, which underlines the importance of the distance separating the jets and the jet velocity in the oscillation phenomenon.

The simulated velocity fields for the various studied oscillator cavities provide additional information on the flow behavior, showing how vortices evolve in the flow at the onset of self-oscillations.

Finally, the oscillator cavities we studied can also be classified as “static mixers” as they provide a rearrangement of the inlet flows without moving parts or external stimuli. For values of Re close to the onset of the self-oscillation phenomenon, a regular temporal rearrangement of the inlet flows was observed in the output channels, but for larger values of Re, the fluid flow in the output channel remains segmented, with only limited mixing. The studied micro-devices cannot consequently be considered for efficient mixing at the microscale, however cavities of adapted geometry can certainly be devised to take advantage of the self-oscillating phenomenon for the creation of efficient micromixers, these will additionally show a relatively low power dissipation as the output channels are of large dimensions compared to the input channels.

As a next step, a thorough linear stability analysis should enable the identification of the governing destabilization mechanism, and determine if this self-sustained oscillation results from the instability of the hyperbolic stagnation line, from the symmetry breaking of the recirculation regions or from the intense shear layers. Additionally, a subsequent weakly nonlinear analysis, which we could not explore numerically in this work, so as to maintain a reasonable computational cost, could confirm the supercritical nature of the bifurcation.

Lastly, since flows in cross-slot geometries are typically known to show hysteretic behavior for certain combinations of the characteristic geometrical parameters [45], a weakly nonlinear analysis could also allow to numerically perform a parametric analysis and investigate possible interactions of the self-sustained regime with eventual non-oscillating symmetry breaking conditions, in particular when the gap separating the two facing inlets, s, and the height, h, approach the inlet width, w.

The authors wish to thank Dr. Lorenzo Siconolfi and Dr. Eunok Yim for their support to this work.

The authors declare the absence of any conflict of interest.

---

[1] S. W. Angrist. Fluid control devices. *Scientific American*, 211(6):80–89, 1964.

[2] H. H. Glaettli. Digital fluid logic elements. In *Advances in computers*, volume 4, pages 169–243. Elsevier, 1964.

[3] J. W. Tanney. Fluidics. *Progress in Aerospace Sciences*, 10:401–509, 1970.

[4] S. Raghu. Feedback-free fluidic oscillator and method, July 3 2001. US Patent 6,253,782.

[5] R. B. Beale and M. T. Lawler. Development of a wall-attachment fluidic oscillator applied to volume flow metering. In *Flow: Its measurement and control in science and industry*, pages 989–996, 1974.

[6] R. D. Stouffer. Liquid oscillator device, April 2 1985. US Patent 4,508,267.

[7] A. Bertsch, S. Heimgartner, P. Cousseau, and P. Renaud. Static micromixers based on large-scale industrial mixer geometry. *Lab on a Chip*, 1(1):56–60, 2001.

[8] M. Anduze, S. Colin, R. Caen, H. Camon, V. Conedera, and T. Do Conto. Analysis and testing of a fluidic vortex microdiode. *Journal of Micromechanics and Microengineering*, 11(2):108, 2001.

[9] S. J. Haward, R. J. Poole, M. A. Alves, P. J. Oliveira, N. Goldenfeld, and A. Q. Shen. Tricritical spiral vortex instability in cross-slot flow. *Physical Review E*, 93(3):031101, 2016.

[10] A. Fani, S. Camarri, and M. V. Salvetti. Investigation of the steady engulfment regime in a three-dimensional t-mixer. *Physics of Fluids*, 25(6):064102, 2013.

[11] X. Niu and Y. K. Lee. Efficient spatial-temporal chaotic mixing in microchannels. *Journal of Micromechanics and Microengineering*, 13(3):454, 2003.

[12] T. S. J. Lammerink, N. R. Tas, J. W. Berenschot, M. C. Elwenspoek, and J. H. J. Fluit-

man. Micromachined hydraulic astable multivibrator. In *Proceedings IEEE Micro Electro Mechanical Systems. 1995*, page 13. IEEE, 1995.

[13] B. Mosadegh, C. H. Kuo, Y. C. Tung, Y. S. Torisawa, T. Bersano-Begey, H. Tavana, and S. Takayama. Integrated elastomeric components for autonomous regulation of sequential and oscillatory flow switching in microfluidic devices. *Nature physics*, 6(6):433, 2010.

[14] S. J. Kim, R. Yokokawa, S. C. Lesher-Perez, and S. Takayama. Constant flow-driven microfluidic oscillator for different duty cycles. *Analytical chemistry*, 84(2):1152–1156, 2011.

[15] S. J. Kim, R. Yokokawa, and S. Takayama. Microfluidic oscillators with widely tunable periods. *Lab on a Chip*, 13(8):1644–1648, 2013.

[16] Z. Li and S. J. Kim. Pulsatile micromixing using water-head-driven microfluidic oscillators. *Chemical Engineering Journal*, 313:1364–1369, 2017.

[17] S. J. Kim, R. Yokokawa, S. C. Lesher-Perez, and S. Takayama. Multiple independent autonomous hydraulic oscillators driven by a common gravity head. *Nature communications*, 6:7301, 2015.

[18] N. S. G. K. Devaraju and M. A. Unger. Pressure driven digital logic in pdms based microfluidic devices fabricated by multilayer soft lithography. *Lab on a Chip*, 12(22):4809–4815, 2012.

[19] T. V. Nguyen, P. N. Duncan, S. Ahrar, and E. E. Hui. Semi-autonomous liquid handling via on-chip pneumatic digital logic. *Lab on a Chip*, 12(20):3991–3994, 2012.

[20] H. M. Xia, Z. P. Wang, W. Fan, A. Wijaya, W. Wang, and Z. F. Wang. Converting steady laminar flow to oscillatory flow through a hydroelasticity approach at microscales. *Lab on a chip*, 12(1):60–64, 2012.

[21] M. N. Tomac and J. Gregory. Frequency studies and scaling effects of jet interaction in a feedback-free fluidic oscillator. In *50th AIAA Aerospace Sciences Meeting including the New Horizons Forum and Aerospace Exposition*, page 1248, 2012.

[22] J. W. Gregory, J. P. Sullivan, G. Raman, and S. Raghu. Characterization of the microfluidic oscillator. *AIAA journal*, 45(3):568–576, 2007.

[23] J. T. Yang, C. K. Chen, I. C. Hu, and P. C. Lyu. Design of a self-flapping microfluidic oscillator and diagnosis with fluorescence methods. *Journal of microelectromechanical systems*, 16(4):826–835, 2007.

[24] C. Xu and Y. Chu. Experimental study on oscillating feedback micromixer for miscible liquids using the coanda effect. *AIChE Journal*, 61(3):1054–1063, 2015.

[25] T. Xie and C. Xu. Numerical and experimental investigations of chaotic mixing behavior in an oscillating feedback micromixer. *Chemical Engineering Science*, 171:303–317, 2017.

[26] C. L. Sun and C. Y. Sun. Effective mixing in a microfluidic oscillator using an impinging jet on a concave surface. *Microsystem technologies*, 17(5-7):911–922, 2011.

[27] C. L. Sun, Y. J. Lin, C. I. Rau, and S. Y. Chiu. Flow characterization and mixing performance of weakly-shear-thinning fluid flows in a microfluidic oscillator. *Journal of Non-Newtonian Fluid Mechanics*, 239:1–12, 2017.

[28] V. Tesař. Oscillator micromixer. *Chemical Engineering Journal*, 155(3):789–799, 2009.

[29] V. A. Denshchikov, V. N. Kondrat'ev, and A. N. Romashov. Interaction between two opposed jets. *Fluid Dynamics*, 13(6):924–926, 1978.

[30] V. A. Denshchikov, V. N. Kondrat'Ev, A. N. Romashov, and V. M. Chubarov. Auto-oscillations of planar colliding jets. *Fluid Dynamics*, 18(3):460–462, 1983.

[31] I. Lashgari, O. Tammisola, V. Citro, M. P. Juniper, and L. Brandt. The planar x-junction flow: stability analysis and control. *Journal of fluid mechanics*, 753:1–28, 2014.

[32] See supplemental material at "link" for videos about the experiments and numerical simulations presented in the present work.

[33] G. B. Lee, C. C. Chang, S. B. Huang, and R. J. Yang. The hydrodynamic focusing effect inside rectangular microchannels. *Journal of Micromechanics and Microengineering*, 16(5):1024, 2006.

[34] J. W. Lottes, P. F. Fischer, and S. G. Kerkemeier. nek5000 web page (2008). *Avialble from: http://nek5000. mcs. anl. gov.*

[35] G. E. Karniadakis, M. Israeli, and S. A. Orszag. High-order splitting methods for the incompressible navier-stokes equations. *Journal of computational physics*, 97(2):414–443, 1991.

[36] D. Sipp, E. Lauga, and L. Jacquin. Vortices in rotating systems: centrifugal, elliptic and hyperbolic type instabilities. *Physics of Fluids*, 11(12):3716–3728, 1999.

[37] S. Ortiz and J.-M. Chomaz. Transient growth of secondary instabilities in parallel wakes: Anti lift-up mechanism and hyperbolic instability. *Physics of Fluids*, 23(11):114106, 2011.

[38] A. Fani, S. Camarri, and M. V. Salvetti. Stability analysis and control of the flow in a symmetric channel with a sudden expansion. *Physics of Fluids*, 24(8):084102, 2012.

[39] J. J. Healey. Destabilizing effects of confinement on homogeneous mixing layers. *Journal of fluid mechanics*, 623:241–271, 2009.

[40] M. P. Juniper. The effect of confinement on the stability of two-dimensional shear flows. *Journal of Fluid Mechanics*, 565:171–195, 2006.

[41] S. J. Rees and M. P. Juniper. The effect of confinement on the stability of viscous planar jets and wakes. *Journal of Fluid Mechanics*, 656:309–336, 2010.

[42] L. Biancofiore and F. Gallaire. The influence of shear layer thickness on the stability of confined two-dimensional wakes. *Physics of Fluids*, 23(3):034103, 2011.

[43] E. Villermaux and E. J. Hopfinger. Self-sustained oscillations of a confined jet: a case study for the non-linear delayed saturation model. *Physica D: Nonlinear Phenomena*, 72(3):230–243, 1994.

[44] E. Villermaux, Y. Gagne, and E. J. Hopfinger. Self sustained oscillations and collective behaviours in a lattice of jets. *Applied Scientific Research*, 51(1-2):243–248, 1993.

[45] N. Burshtein, A. Q. Shen, and S. J. Haward. Controlled symmetry breaking and vortex dynamics in intersecting flows. *Physics of Fluids*, 31(3):034104, 2019.